High-Resolution Imaging of the Near-Nozzle Region of a Non-Reacting Spray

M.J. Tess*, M.S. Kurman, L.G. Bravo and C.-B. Kweon
Vehicle Technology Directorate
U.S. Army Research Laboratory
Aberdeen Proving Ground, MD 21005 USA

Abstract

High-fidelity computational fluid dynamics models of diesel sprays require validation from high-quality experimental data. In particular, detailed physical models of the initial breakup and atomization of a diesel spray require information on the droplet sizes and instability length scales. Depending on the atomization mode, the acquisition of such experimental data can be challenging because the relevant time and length scales test the resolution capabilities of modern imaging systems. This paper presents high-resolution backlit image data acquired in the near-nozzle regions of non-evaporating and non-reacting sprays of iso-paraffinic kerosene and n-dodecane fuels. The in-plane resolution of the image system was measured using a scanning edge technique to quantify the line spread function. The jets were issued from three different single axial-hole common rail diesel injectors into a quiescent, high-pressure environment at tip velocities ranging from 9−165 m/s. For the quasi-steady phase of the injection event, the Reynolds numbers ranged from 3,000−36,000 with an Ohnesorge number of 0.04-0.06, indicating the jets were in the second wind induced and full atomization breakup modes. The results provide detailed information about the structure of diesel sprays that may be used to validate CFD models.

*Corresponding author: michael.tess@us.army.mil

Introduction

The performance of modern, direct-injection compression-ignition engines greatly depends on the fuel injection strategies designed to meet power and emissions targets over the product life-cycle. Accordingly, recent trends in the light, medium, and heavy-duty engine industries have tended towards very high pressure (exceeding 2000 bar) fuel injections using small orifice diameter (less than 130 µm) multi-hole nozzles. A critical step during the initial stages of the overall engine development effort for these advanced engine technologies is an understanding of the spatial and temporal evolution of the air-fuel mixture formation processes because of their effects on combustion quality and pollutant formation. Furthermore, manufacturers are increasingly reliant on complex computational fluid dynamics (CFD) models to reduce the time and development and costs associated with bringing new engine technologies to the market. Computational models, of course, require high-quality experimental data across a wide range of conditions to validate their accuracy and promulgate their use as a predictive tool. These considerations motivate the experimental results presented in this paper investigating the flow of a non-evaporating fuel spray in the near-nozzle region. The injection system boundary conditions, while not near the capabilities of a state-of-the-art automotive diesel engine, were selected to make the computing hours tractable for a parallel CFD effort that aimed to model these sprays. Interested readers are encouraged to see the companion paper, also submitted to the 27th ILASS Americas conference, for the results of the detailed numerical simulations [1].

In recent years, much research has been devoted to the development of high-resolution imaging techniques of the near-nozzle region [2]. Technological advances such as ballistic imaging [3,4] and x-ray radiography [5,6] have helped researchers investigate the transient morphology of high-velocity sprays with excellent fidelity. Quantitative characteristics such as the axial velocity field [7], droplet sizes [8], and liquid volume fraction [9] have been measured experimentally using x-ray techniques. Simpler optical diagnostics like backlit imaging have also proven to be highly informative when probing the near-nozzle region by coupling long-distance microscope lenses to high-speed [10] and ultra high-speed cameras [11]. The present research implemented the backlit imaging technique using a high-speed camera system capable of 10 million frames per second at 50 ns exposure duration.

The development of detailed physical models for the break-up and atomization processes of liquid sprays presents numerous challenges for both experimentalists and modelers because the magnitudes of the time and length scales of interest are exceedingly short. It is also recognized that the time and length scales vary inversely with the fuel velocity; and, trends to downsize the orifice diameter further reduce the multi-phase flow length scales. Hence, in order to experimentally image the transient spray features given the optical trade-off between recording speed and contrast resolution for conventional imaging techniques, several of the injection pressure conditions in this research, while unrealistic for modern diesel engine operation, were purposely selected to maximize the time and length scales. The Reynolds (*Re*) and Weber (*We*) numbers ranged from 3,000−9,000 and 36,000−146,000, respectively, which categorized the sprays in the second wind induced breakup regime. For comparative evaluation purposes, limited data were acquired at injection pressures exceeding 1000 bar, or Re = 36,000 and We = 1,800,000. Finally, the ambient conditions for all experiments resulted in a fuel to ambient density ratio ρ_f / ρ_a = 33, where aerodynamic forces dominate the breakup mechanism [12].

Experimental Setup

The spray experiments were performed in a dual-walled, constant-pressure flow chamber using a simple backlit imaging setup as depicted in Figure 1. Orthogonal and axial optical access to the fuel spray was provided by three 147 mm diameter, 85 mm thick UV-grade fused silica (UVFS) windows. The ambient gas composition was dry air (78% nitrogen, 21% oxygen, plus 1% trace constituents) at a temperature and pressure of 300 K and 20 bar, respectively, giving an ambient density ρ_a equal to 23 kg/m^3. The fuel injector, described in detail in the next section, was mounted to the chamber using a water-cooled fixture maintained at 280 K. Although the fuel temperature at the tip was not measured directly, the dwell time between injection events was sufficiently long for the fuel in the injector body to equilibrate to the temperature of the cooling water, thus approximating an engine cold-start condition.

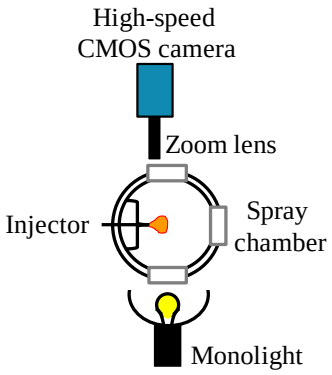

Figure 1. Illustration of the spray chamber and backlit imaging optical setup.

Two fuels were used for the experiments: an iso-paraffinic kerosene (IPK) and n-dodecane. The IPK sample (POSF 7629) was a coal-to-liquid jet fuel produced by Sasol in a Fischer-Tropsch process; the n-dodecane was a 99%-pure reagent grade commercial product. The physical properties for both fuels, with the exception of surface tension, were generated from the NIST database [13], for which IPK was represented by a four-component surrogate mixture [14]. The surface tension for both fuels was found in [15], for which the values of n-dodecane and IPK were assumed to be equal based on the volume fraction of the surrogate mixture constituents.

The injection events were imaged with a Shimadzu HPV-X frame transfer CMOS camera and a Navitar long-working distance 12× zoom lens. The camera was capable of recording a maximum of 256 full-frame images (400 × 250 pixels) at speeds up to 10 million frames per second with a 50 ns exposure. The working distance of the zoom lens and stand-off distance of the spray chamber constrained the maximum achievable optical magnification. In the base configuration, the spatial resolution was limited to 9.35 µm/pixel; therefore, a set of three 27.5 mm extension tubes were stacked together with the lens to achieve a resolution of 5 µm/pixel, or equivalently, a magnification ratio m = 5, for a 2 mm × 1.25 mm field of view size. The image system resolution is further quantified in the section below regarding image resolution analysis.

The light source was a Photogenic model PL2500 1000 W·s photographic flash unit with color-corrected flash tube, parabolic reflector, and 75 mm diameter barrel attachment. The peak light intensity duration equaled 550 µs, followed by a linear decay for a total flash duration of approximately 1500 µs. A digital delay generator was used to synchronize the timing of the flash unit to the fuel injection event and camera recording trigger for relatively consistent lighting, although at long injection durations (greater than 1.5 ms) the overall signal intensity of the last recorded frames decreased. Considering the flash duration and the 256-frame limit of the camera, the recording speed and exposure duration were adjusted throughout the course of the experiments to capture the time period of interest, such as the full spray event from the start to the end of injection, or the transient phenomena during needle opening and closing.

Fuel Injectors and Rate Measurements

Table 1 lists the geometric specifications for the three types of injectors used for the experiments. Most experiments were performed with the Bosch CRIN-18 common-rail fuel injectors featuring sharp-edged, single-axial hole nozzles having either 90 or 147 µm (nominal) orifice diameters. A modified Delphi injector with a negative k-factor, 50 µm (nominal) orifice diameter single-axial hole nozzle was used for two conditions [16].

Table 1. Injector specifications

	Injector #1	Injector #2	Injector #3
Injector type	Bosch CRIN-18	Bosch CRIN-18	Delphi DFI 1
Nozzle type	sac	sac	sac
Orifice orientation	axial	axial	axial
d (nominal) [µm]	90	147	50
d (measured) [µm]	102	168	67
l/d	7.4	4.5	9.0
Orifice edges	sharp	sharp	sharp
k-factor	N/A	N/A	-3

Microscopic images of the Bosch injector nozzle tips were acquired with a SPOT Idea 5 megapixel camera mounted to an Olympus SZH10 microscope and 2× objective lens. A scaling calibration was performed by imaging a clear glass plate imprinted with opaque circles ranging in size from 10 – 200 µm diameter. The total magnification achieved with this setup was m = 7 (0.3 µm/pixel). A circle was then fit to the orifice outlet to determine the actual orifice diameter. Figure 2 shows the fitted circle overlaid on the microscope images of the (a) 90 µm orifice outlet and (b) 147 µm orifice outlet.

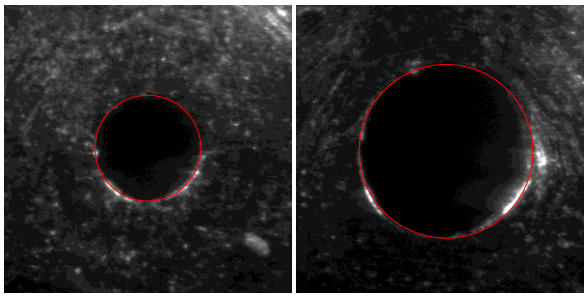

(a) (b)

Figure 2. Microscope images of the nozzle tip overlaid with a circle fitted to the orifice outlet for the (a) 90 µm (nominal) orifice and (b) 147 µm (nominal) orifice.

The measured orifice diameters for these nozzles are listed in Table 1. The uncertainty for this image-based measurement technique is estimated at ±1.2 µm. For reference, an x-ray imaging technique of the 90 µm (nominal) orifice resulted in a measured orifice diameter equal to 96 µm; and a three-dimensional laser scan of the 147 µm (nominal) orifice gave an actual diameter of 167.8 µm. The 50 µm (nominal) orifice was meas-

ured with a Vickers M41 research measurement microscope [16].

The mass flow rate for each operating condition with IPK fuel was measured with a tube-type rate instrument [17] maintained at 20 bar back pressure to duplicate the pressure boundary conditions of the image data. Rates of injection (ROIs) were averaged over 100 shots, and shot-to-shot variation of the injected mass was less than 1% for all conditions. Figure 3 shows the average ROI profiles and injector solenoid current versus the time after start of injection command (SOIC) for three pressure drops across the 90 µm (nominal) diameter orifice of 75, 130, 200 bar, all at a constant solenoid energizing time of 0.7 ms. Throughout this paper, the times for the ROI and image data are relative to SOIC because it provided a common trigger point for the two sets of experiments. Efforts were made to correlate the start of injection for the image data to the start of injection for the ROI data, but significant shot-to-shot variability existed in the image data on a time scale much less than the 10 µs resolution of the ROI data. For future work, the sampling rate will be increased to at least match the camera frame rate. Additionally, at least for high-speed experiments, the distance between the injector orifices and the pressure sensor in the rate meter must be accounted for when measuring the hydraulic delay time between the start of command and start of injection.

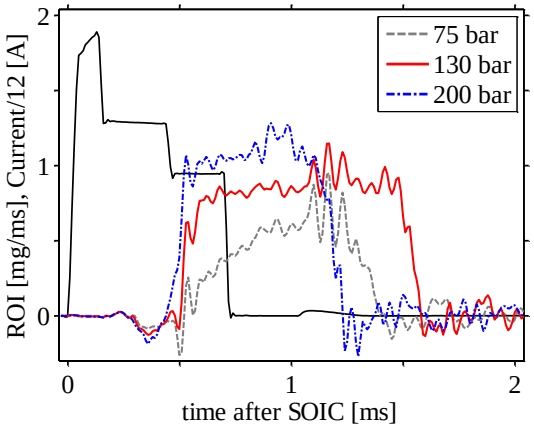

Figure 3. Rates of injection and injector solenoid current (black trace) versus the time after start of injection command (SOIC) for the 90 µm (nominal) diameter orifice injector at three differential pressures (P_{rail} minus P_a).

As explained in the Introduction, the injection pressures were kept low in most cases to facilitate CFD-modeling and explore the atomization mechanisms at various operating points, hence providing comprehensive analysis of the physics. The ROIs in Figure 3 suggest that the injector servo-hydraulic flow circuit behaved inconsistently at such low rail pressures due to a force imbalance on the needle. This is evident in the ramping rate profile for the 75 bar injection pressure case ($\Delta P = P_{rail} - P_a$), and the significantly different end of injection times. At higher injection pressures with the 90 µm injector, the ROIs exhibited a square rate shape that is a well-known characteristic of single-hole nozzles. The 147 µm injector behaved slightly different at low injection pressure, requiring a minimum pressure drop of 102 bar in order to lift the needle off the seat. Finally, the flow rate fluctuations observed in Figure 3 during the quasi-steady period of the injection event, with magnitudes that were as large as ±40% of the mean, were believed to be artifacts of oscillatory needle motion [18], acoustic wave propagation phenomena [19], and cavitation at the pressure sensor.

Image Resolution Analysis

Before presenting the image data, it is important to discuss the size limits of what can realistically be resolved. Light diffraction effects and lens imperfections control the actual resolving power of the optical system to distinguish droplets or other small-scale structures of the spray from the background. Therefore, the true resolution of the optical system was evaluated by scanning a knife edge across the field of view to measure the step response function (SRF). The SRF was well-approximated by an error function, as shown by the fitted black curve in Figure 4. The line spread function (LSF), which is the derivative of the SRF, is a more accurate metric of spatial resolution than the pixel spacing [20]. The LSF is a Gaussian function with characteristic width σ_{LSF}, which equaled 11.2 µm for the plane of best focus (defined as $y = 0$) in the present spray experiments. The Nyquist criterion suggests that at least two data points are required to spatially measure (by counting pixels) a characteristic length without aliasing. In these experiments, however, the spatial distance of two pixels was less than σ_{LSF}, meaning the smallest resolvable physical feature of the spray was at least three pixels, or 15 µm, across its smallest dimension. For comparison, Crua *et al.* achieved 0.57 µm/pixel resolution (although σ_{LSF} was not reported) using a long range microscope lens in their work measuring the drop sizes of a diesel spray [21]. For these reasons, macroscopic spray parameters, including spray tip penetration, tip velocity, and spreading angle, were the only features quantified during the post-processing of the image data.

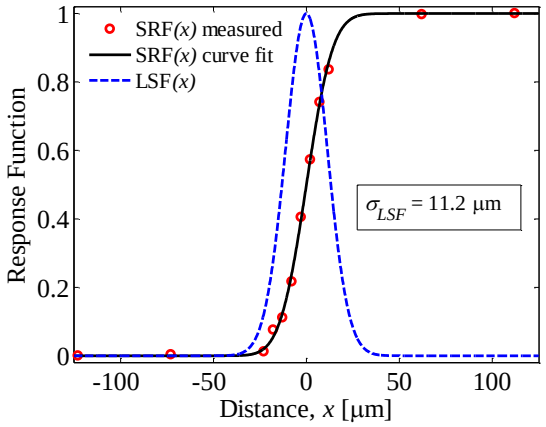

Figure 4. Step response function (SRF) and line spread function (LSF) of the long-distance microscopy optical system.

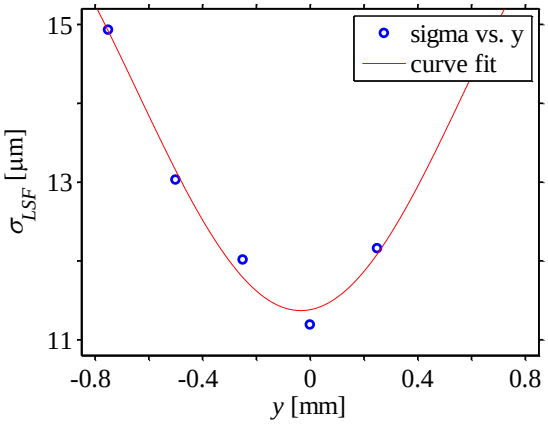

Figure 5. Characterstic width of the Gaussian line spread function (σ_{LSF}) versus relative distance y along the optical axis from the plane of best focus.

Backlit imaging is a line-of-sight technique, and droplets shed from the spray may appear blurred at least partially due to imaged objects located in planes outside the depth of field of the imaging system. Accordingly, the depth of field was evaluated by translating the knife edge along the optical axis y, or in other words, closer to and away from the plane of the camera sensor. Figure 5 shows the results of this analysis in terms of the measured σ_{LSF} versus distance relative to the plane of best focus at $y = 0$, where negative values were closer to, and positive values further away from, the image plane at the sensor. The data show that the spatial resolution decreased approximately 9% at each 250 µm interval away from the image plane. Assuming the object plane bisected the fuel plume along the spray axis, defined by the axial centerline of the injector orifice, the surface features of the unbroken liquid core should appear sharp for even the largest orifice diameter injector (d = 168 µm), to within the limits of the LSF discussed previously.

Image Processing

The image data were post-processed with an ARL-modified version of Sandia National Lab's Engine Combustion Network (ECN) high-speed video processing MATLAB code [22]. In brief, the processing algorithm first applies a simple threshold function to define the contiguous regions of the spray [23]. With the spray boundary determined, the penetration length and local dispersion angle are calculated using the iterative method developed by Naber and Siebers [24]. Figure 6 shows a sample for a processed image outlining the major features of the spray, including the spray boundary, centerline, dispersion angle, and tip penetration.

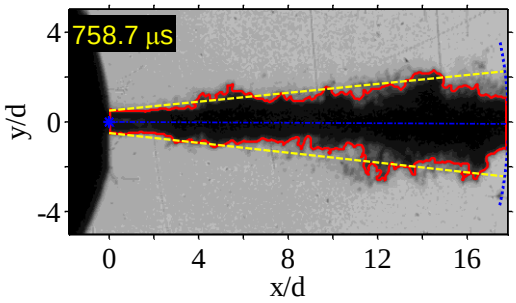

Figure 6. Example of a processed image showing the spray boundary (red outline), orifice origin (blue symbol), spray angle (yellow lines), spray centerline (dot-dash blue line), and spray penetration (dotted blue arc). Condition: 90 µm nozzle, ΔP = 75 bar, IPK fuel, ρ_a = 23 kg/m^3, and T_a = 300 K.

Spray Results

Table 2 lists the conditions and relevant dimensionless numbers for the nine spray cases examined with high-speed imaging. The measured orifice exit diameter and Bernoulli velocity were used for the calcula-

tions, so the dimensionless numbers describe the average spray at the nozzle exit during the quasi-steady period of mass flow through the orifice. The ROIs in Figure 3 indicate that the flow reached steady-state within 200 µs after the start of injection. The Ohnesorge number suggests that the cases with injection pressures less than 1000 bar were in the second wind-induced breakup regime.

Table 2. Description of spray cases in terms of fluid mechanic properties

Case	d	ΔP	Fuel	Re	We	Oh^{-1}
	[µm]	[bar]		$\times 10^3$	$\times 10^4$	
1	90	75	IPK	4.9	5.5	21
2	90	130	IPK	6.5	9.5	21
3	90	200	IPK	8.0	14.6	21
4	50	75	IPK	3.2	3.6	17
5	50	1175	IPK	12.8	56.2	17
6	147	102	IPK	9.5	12.2	27
7	147	1500	IPK	36.3	180	27
8	90	75	$C_{12}H_{26}$	5.5	5.7	23
9	90	130	$C_{12}H_{26}$	7.2	9.8	23

Figure 7 shows selected images from a single injection event recorded at 416,667 frames/sec from the 90 µm (nominal) orifice nozzle at ΔP = 75 bar injection pressure with IPK fuel. The time of image acquisition annotated in the upper left of each image is relative to SOIC, and the axes coordinates are normalized by the measured orifice outlet diameter. As seen in the image acquired at 527.2 µs, a few isolated droplets were ejected from the orifice prior to the main injection event. This was a common phenomenon observed to occur primarily at the lowest injection pressures. The actual start of injection commenced with a continuous column of fuel appearing to have laminar flow characteristics. The image at 642.4 µs shows the deforming effects of aerodynamic drag forces on the spray tip, giving the appearance of a mushroom cap feature. Close inspection of this image also indicates that the diameter varied slightly along the length of the solid fuel core. At 743.2 µs, wave instabilities appeared to propagate with varying amplitude on the surface of the spray, with the strongest instabilities observed downstream of the orifice at x/d ~ 5. A short time later, ligaments and other structures appear to shed the original instability, resulting in primary and secondary breakup downstream from the nozzle exit observed at 755.2 µs. The onset of breakup advanced upstream in the flow at later times, seen in the images acquired at 762.4 µs and 769.6 µs, as full atomization coincided with the increased flow velocity from the injector needle continuing to lift off the seat. At 925.6 µs, the onset of breakup was seen to stabilize at around x/d ~ 2 for this condition, and the spray achieved a quasi-steady atomization breakup regime. The liquid core was no longer visible because of the dense layer of droplets on the spray boundary. A short time later, at 1009.6 µs, the onset location appeared to move back downstream, signifying the decreased flow velocity from the end of injection transition. The flow velocity was so low that the final movie frames suggest the last parcels of fluid failed to break up before exiting the field of view.

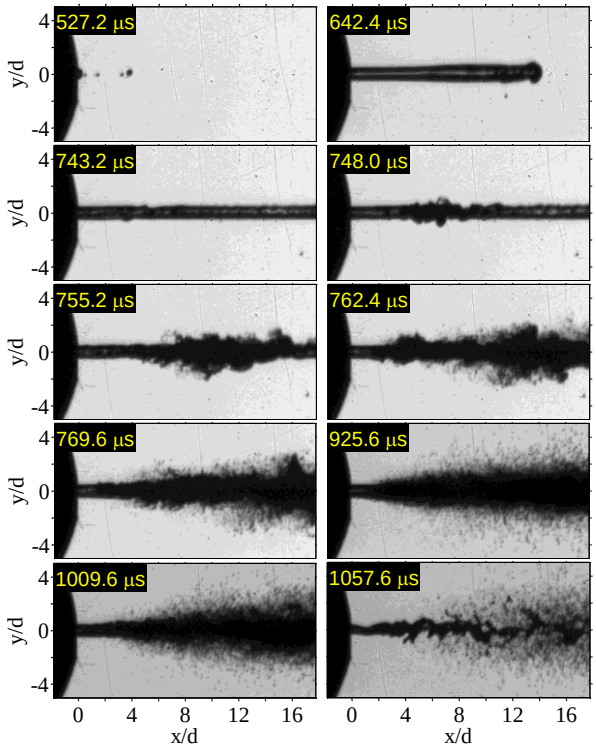

Figure 7. Sequence of images showing a single injection event from the start to the end of injection for the 90 µm (nominal) diameter single-hole nozzle at ΔP = 75 bar with IPK fuel. The time in the upper left corner is relative to the start of injection command.

Figure 8 shows the effects of injection velocity on the breakup process for the 90 µm (nominal) diameter nozzle with IPK fuel. The sequence of four images in the left column were acquired at ΔP = 130 bar injection pressure, and the sequence in the right column were for ΔP = 200 bar injection pressure. In consideration of the higher spray velocity at these pressures, the recording rate was increased to 10M frames/second at 50 ns exposure duration to freeze the flow as much as possible, although some blurring still occurred due to vibrations in the optical mounting setup. Where possible, the images in Figure 8 were taken from the same movie to exemplify the different stages of the spray development process, from the initial penetration of the jet

across the field of view to full atomization. The camera's total frame limit of 256 frames per recording translated to a total duration of 25.6 µs at the 10M frames/second setting, so some frames in the sequence came from a different movie.

The increase in aerodynamic drag forces at higher velocity caused much more deformation in the head of the spray, inducing primary and secondary breakup to occur in the jet tip for the 200 bar case. The spray at ΔP = 130 bar apparently progressed through similar steps as the 75 bar case leading up to full atomization, but in a much more compressed time scale. The Reynolds number of the 200 bar case (~8000) suggests the flow had transitioned to fully-developed turbulent pipe flow at the spray exit, resulting in a near fully atomized spray at the plane where the spray exited the orifice. This was also evident in the image data shown in Figure 8, although the location of the onset of breakup still appeared to propagate upstream towards the nozzle exit between 364.0 µs and 371.8 µs. It was difficult to compare the sizes of the droplets in the images in Figures 7 and 8 because they were only two to three pixels in diameter, which was previously explained to be the lower limit of the imaging system resolution. Regardless, the fully atomized spray, seen in the images acquired at 967 µs for the 130 bar case and 700.9 µs for the 200 bar case, was clearly more optically dense. Future work will utilize an ultra-high speed framing camera to learn more about the spray structure in this region.

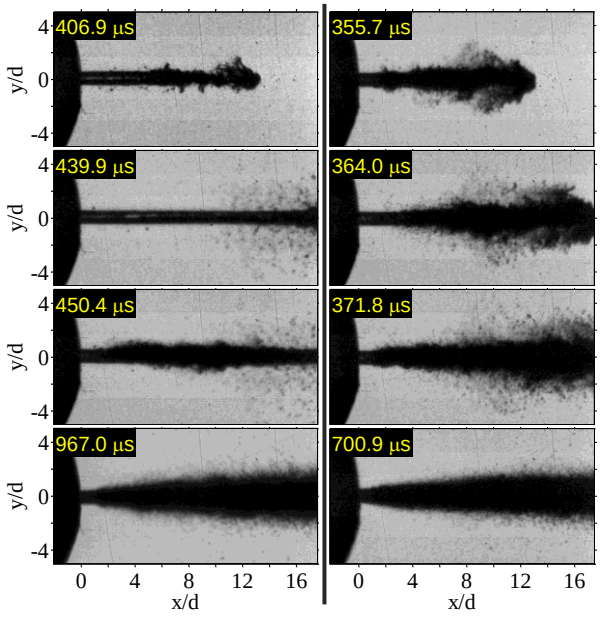

Figure 8. Sequence of images showing the effects of injection velocity on the spray breakup process for the 90 µm (nominal) diameter nozzle with IPK fuel. Left column: ΔP = 130 bar. Right column: ΔP = 200 bar.

Figure 9 presents an analogous sequence of images showing the effect of orifice diameter on the near-nozzle spray development and breakup processes from initial penetration to full atomization. The sequence of four images in the left column were acquired with the 50 µm (nominal) orifice nozzle at ΔP = 75 bar injection pressure, and the sequence in the right column were taken with the 147 µm (nominal) orifice nozzle at ΔP = 102 bar injection pressure. Recall that the minimum pressure drop for the needle to lift off the seat with the 147 µm injector was 102 bar. The face of the 50 µm nozzle was ground flat for manufacturing reasons, but appeared rounded at early times after start of injection because of a fuel leak across the needle and seat. The first parcels of fluid issued from this nozzle therefore had to penetrate through a stagnant layer of fuel on the tip, which was drawn into the spray and shed from the tip at later times during the injection event.

The head of spray for the 147 µm nozzle showed a more distinct Rayleigh-Taylor instability because of the larger frontal area of the liquid column. The wave instability features and primary breakup structures were clearly evident in the spray images acquired at 668.8 µs and 655.5 µs for this nozzle (time difference due to shot-to-shot variability in the start of injection for different movies). The spray from the 50 µm nozzle, despite the lowest Reynolds number out of all the cases, appeared to initially breakup 4 - 8 nozzle diameters

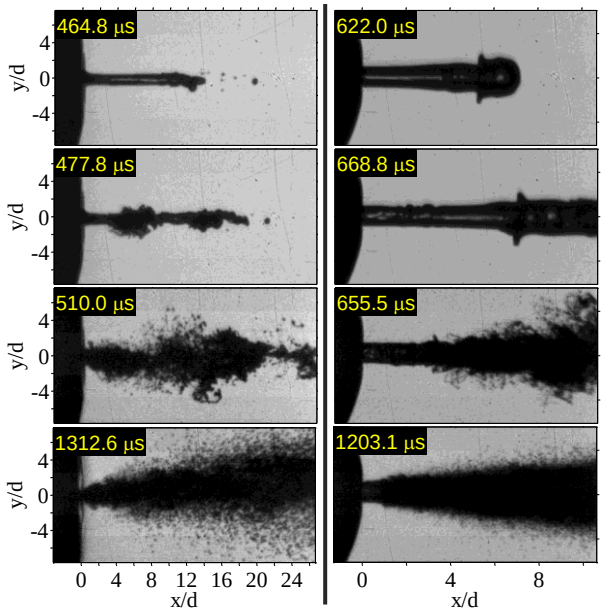

Figure 9. Sequence of images showing the effects of orifice diameter on the spray breakup process with IPK fuel. Left column: 50 µm (nominal) orifice diameter, ΔP = 75 bar. Right column: 147 µm (nominal) orifice diameter, ΔP = 102 bar.

downstream of the exit, which was consistent with the 90 µm orifice at 75 bar pressure drop. The liquid column almost completely broke up for this nozzle at 510.0 µs, and the droplets appear larger than the 90 µm nozzle at the same pressure, perhaps because of the negative k-factor. More investigation is needed to understand these phenomena.

The final sequence of images, Figure 10, shows sprays of the single-component fuel n-dodecane injected from the 90µm orifice diameter nozzle at two different injection pressures. The sequence of four images in the left column were acquired at ΔP = 75 bar injection pressure, and the sequence in the right column were for ΔP = 130 bar injection pressure. The physical properties for these two fuels are within 10% of each other, suggesting that the non-evaporating sprays should also be very similar. Compared to the images in Figure 7 and the left column of Figure 8, it is seen that the spray features are also phenomenologically similar. In all cases, the liquid column penetrates across the field of view before primary breakup appears to occur through wave instability mechanisms, followed by the onset of full atomization at one to two nozzle diameters downstream from the exit.

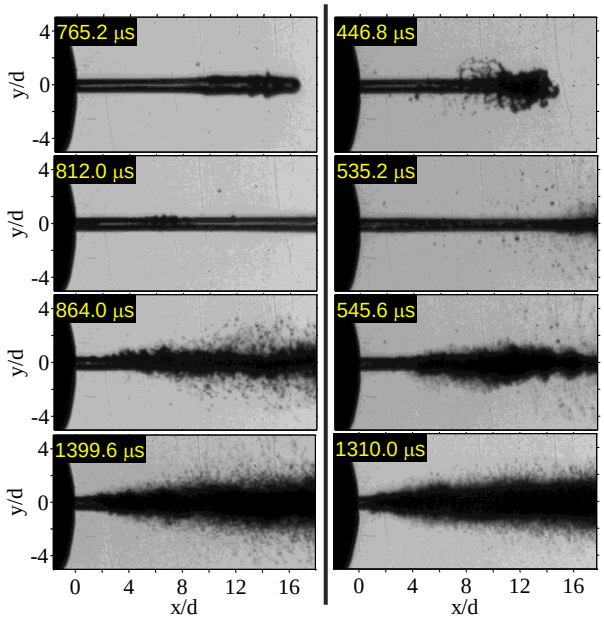

Figure 10. Sequence of images showing the effects of injection velocity on the spray breakup process for the 90 µm (nominal) diameter nozzle with n-dodecane fuel. Left column: ΔP = 75 bar. Right column: ΔP = 130 bar.

The spray tip penetration S_{tip} results are plotted versus time after start of injection in Figure 11 for the 90 µm nozzle with IPK at the three injection pressures. The time reference was changed to eliminate the shot-to-shot variation in start of injection timing, which was on the order of 10 µs at low injection pressures. The symbols show the tip penetration for up to 10 different injection events recorded per condition. Lines were then fit to the penetration data for each injection event, and the average of the slopes are plotted for each condition as the solid black lines.

Clearly, the tip penetration is linear, with only a 3-5 µs segment of non-linear ramp up time at the very start of injection for the 200 bar injection pressure case. The scatter in the data points for the 75 bar injection pressure case was partially due to the detection of droplets ejected ahead of the continuous liquid column, and from instability in the needle motion due to the balance of forces between the hydraulic and spring forces. This was most evident for the 147 µm nozzle (not shown): the penetration data at 102 bar pressure (minimum injection pressure) were basically non-linear, whereas the data 1500 bar pressure showed consistent, excellent linearity.

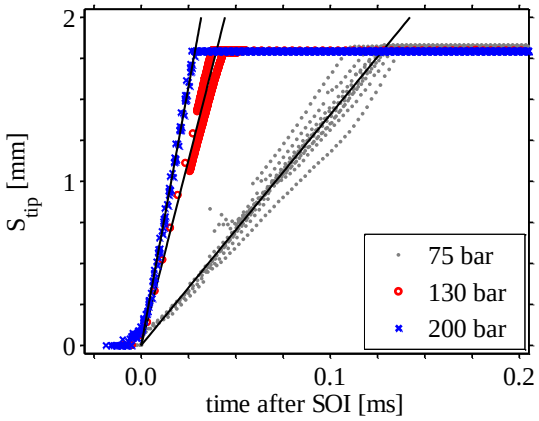

Figure 11. Effect of injection pressure on the spray tip penetration (S_{tip}) versus time after start of injection (SOI). Symbols: experiments; lines: mean of linear fits to the sets of single injection event data.

Table 3 lists the average tip velocity $\overline{U}_{tip}$ with the 95% confidence interval, calculated from the slopes of the fitted lines as described above, and the theoretical Bernoulli velocity $\overline{U}_B$ based on the pressure drop across the orifice, for all nine cases. Tip velocity data were not available for the 50 µm nozzle at 1175 bar injection pressure because the movies were not recorded at a high enough frame rate to get multiples frames with the spray tip in the field of view; additionally, the velocity reported for the 147 µm, ΔP = 102 bar case is unreliable as previously discussed. The tip velocity for IPK and n-dodecane were essentially identical at 75 bar pressure, but lower for n-dodecane at 130 bar pressure. Also, the velocity of the 50 µm nozzle at the same pressure drop was approximately double that of the 90 µm nozzle, probably because of servo-hydraulic effects.

Overall, the tip velocity was approximately 10-25% of the Bernoulli velocity, as expected, because of the transient nature of the flow at the start of injection.

Table 3. Maximum theoretical velocity and measured average tip velocity

Spray boundary conditions	$\overline{U}_B$ [m/s]	$\overline{U}_{tip}$ [m/s]
d =102 µm, ΔP=75 bar, IPK	140	14.1 ± 0.1
d =102 µm, ΔP=130 bar, IPK	184	45.1 ± 0.6
d =102 µm, ΔP=200 bar, IPK	228	63.0 ± 2.3
d = 67 µm, ΔP=75 bar, IPK	140	30.0 ± 2.6
d = 67 µm, ΔP=1175 bar, IPK	553	N/A
d =147 µm, ΔP=102 bar , IPK	163	9.3 ± 0.5
d =147 µm, ΔP=1500 bar , IPK	625	164.7 ± 10.3
d =102 µm, ΔP=75 bar, $C_{12}H_{26}$	140	13.7 ± 0.3
d =102 µm, ΔP=130 bar, $C_{12}H_{26}$	185	35.9 ± 2.7

It was also of interest to determine how the measured tip velocity compared to the mass-average injection velocity determined from the ROI data, assuming a unity discharge coefficient. Figure 12 plots the mass-average injection velocity at the orifice exit U_{inj} versus time after start of injection command for the same ROIs from Figure 3. The time axis was scaled to the same total time interval (0.225 ms) as Figure 11 to highlight the transient period at the start of injection. The data suggest that the initial parcels of fluid were injected with low velocity, continuously followed by accelerating fluid parcels up until the point where the full injection pressure was realized. The image data, on the other hand, indicate that the velocity at the tip remained constant over this time interval, suggesting a balance between the acceleration force imparted on the fluid parcels immediately downstream of the nozzle and the viscous, inertial and drag forces acting on the developing spray up to the tip. The accelerating fluid at the nozzle exit partially explains the wave instabilities observed in the image data, such as the image acquired at 668.8 µs of Figure 9.

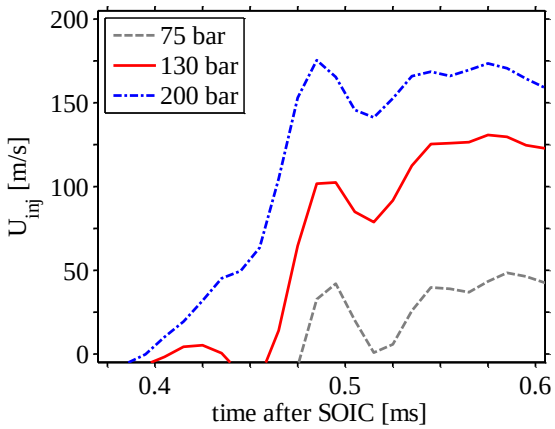

Figure 12. Mass-average injection velocity U_{inj} versus time after SOIC for the time period shortly after the start of injection.

Figure 13 plots the average spray spreading angle θ versus time after SOIC for five cases (labeled 4-8 in Table 2) to demonstrate the effects of orifice geometry and injection pressure. The spreading angle for n-dodecane and IPK (not shown) were found to be identical at comparable injection pressures, so case 8 using n-dodecane was selected for the figure. First, there appears to be a small effect from injection pressure, although this trend is most likely confounded by the image processing algorithm's ability to distinguish the spray boundary at low injection pressures. The example in Figure 6 (ΔP = 75 bar) confirms that, in some instances, the detected spray boundary included less optically dense regions. At higher injection pressures, such as the image at the bottom left of Figure 8, the high density of droplets on the spray boundary made this ambiguity non-existent. Other spray studies in the literature [24-26] do not show any significant effect from injection pressure. Second, orifice geometry significantly influences the spreading angle. The spray angle for the 50 µm (nominal) orifice diameter nozzle, which featured a negative k-factor, was approximately two times larger than the spray angle for the 147 µm (nominal) orifice diameter nozzle at their respective high injection pressure cases. Turbulence wall effects in the nozzle are expected to cause the turbulence intensity and turbulent kinetic energy profiles to grow radially.

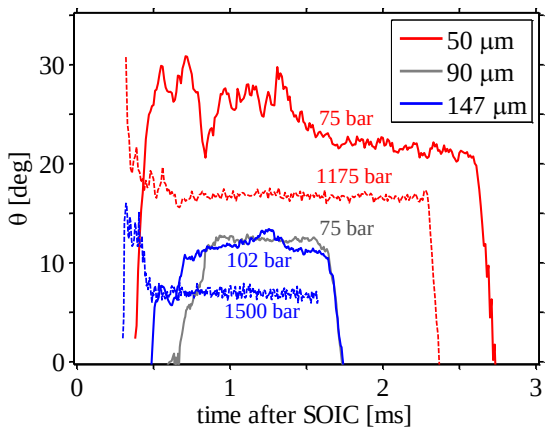

Figure 13. Near-nozzle average spray spreading angle (θ) versus time after SOIC, demonstrating the effects of orifice geometry and injection pressure.

Conclusions

The effects of injection pressure, orifice geometry, and fuel composition on the transient structure of a non-evaporating spray were investigated with a backlit imaging technique. High-speed movies of the near-nozzle region were acquired at recording rates up to 10 million frames per second, enabling measurement of the spray tip penetration, velocity, and spreading angle. The spray tip penetration was found to be linearly dependent on injection pressure within the limited field of view, which ranged from 10-26 nozzle diameters downstream of the jet origin, depending on the orifice diameter. The spray tip velocities were compared to the theoretical velocity at the jet exit and the mass-average velocity derived from rate of injection measurements. Finally, the orifice geometry was found to significantly affect the spray spreading angle during the fully-developed phase of the injection event. No significant differences in the non-evaporating spray structure were found between Sasol IPK jet fuel and n-dodecane. The results provide detailed information about the structure of pressure-atomized sprays that may be used to study the physics of spray breakup, and thus aid in the development and validation of CFD models.

Nomenclature

P	pressure
SOI	start of injection
SOIC	start of injection command
U	velocity
x	spray axial direction
y	spray transverse direction
θ	spray spreading angle
ρ	density
σ	line spread function width

Subscripts

a	ambient
B	Bernoulli
inj	injection
l	liquid

Acknowledgements

This research was supported in part by an appointment to the U.S. Army Research Laboratory Postdoctoral Fellowship Program administered by the Oak Ridge Associated Universities through a contract with ARL. The authors thank Mr. Todd Rumbaugh of Hadland Imaging for technical assistance with the imaging setup, and the use of the Shimadzu HPV-X camera system and light source. Dr. Tim Edwards of the U.S. Air Force Research Laboratory provided the IPK jet fuel.

References

1. Bravo, L., Kim, D., Tess, M., Kurman, M., Ham, F., and Kweon, C.-B., *27th Annual Conference on Liquid Atomization and Spray Systems*, Raleigh, NC, May 2015.
2. Linne, M., *Progress in Energy and Combustion Science* 39:403-440 (2013).
3. Linne, M., Paciaroni, M., Hall, T., and Parker, T., *Experiments in Fluids* 40:836-846 (2006).
4. Schmidt, J.B., Schaefer, Z.D., Meyer, T.R., Roy, S., Danczyk, S.A., and Gord, J.R., *Applied Optics* 48:B137-B144 (2009).
5. Kastengren, A.L., Powell, C.F., Wang, Y.J., Im, K.S., and Wang, J., *Atomization and Sprays* 19:1031-1044 (2009).
6. Kastengren, A.L., Powell, C.F., Arms, D., Dufresne, E.M., and Wang, J., *22nd Annual Conference on Liquid Atomization and Spray Systems*, Cincinnati, OH, May 2010.
7. Liu, Z., Im, K.-S., Xie, X., Wang, Y., Zhang, X., Moon, S., et al., *22nd Annual Conference on Liquid Atomization and Spray Systems*, Cincinnati, OH, May 2010.
8. Powell, C.F., Duke, D., Kastengren, A., and Ilavsky, J., *25th Annual Conference on Liquid Atomization and Spray Systems*, Pittsburgh, PA, May 2013.
9. Pickett, L.M., Manin, J., Kastengren, A., and Powell, C., SAE Technical Paper 2014-01-1412 (2014).
10. Manin, J., Bardi, M., Pickett, L.M., Dahms, R.N., and Oefelein, J.C., *THIESEL*, Valencia, Spain, September 2012.
11. Crua, C., Shoba, T., Heikal, M., Gold, M., and Higham, C., SAE Technical Paper 2010-01-2247 (2010).
12. Faeth, G.M., Hsiang, L.P., and Wu, P.-K., *International Journal of Multiphase Flow* 21:99-127 (1995).

13. NIST Reference Fluid Thermodynamic and Transport Property Database (REFPROP): Version 9.1.
14. Colket, M., Zeppieri, S., Dai, Z., Kim, W., Hollick, H., and Hautman, D., "Alternative Fuels Modeling for Navy Applications," ONR Contract N00014-12-C-0408, Final Report, June 2013.
15. Luning Prak, D.J., Alexandre, S.M., Cowart, J.S., and Trulove, P.C., *Journal of Chemical and Engineering Data* 59:1334-1346 (2014).
16. Jerovsek, J., and Dorner, M., "Development of Micro JP-8 Fuel Injection Systems for Small Unmanned Aerial and Ground Engines," SBIR Phase I Final Report, Contract #W911QX-14-C-0048, 2014.
17. Bosch, W., SAE Technical Paper 660749 (1966).
18. Kastengren, A.L., Tilocco, F.Z., Powell, C.F., Manin, J., Pickett, L.M., Payri, R., and Bazyn, T., *Atomization and Sprays* 22:1011-1052 (2012).
19. Manin, J., Kastengren, A., and Payri, R., *Journal of Engineering for Gas Turbines and Power*, 134:122801-1 – 122801-10 (2012).
20. Clemens, N.T. Flow Imaging, in *Encyclopedia of Imaging Science and Technology*, John Wiley and Sons, 2002, p. 390-419.
21. Crua, C., de Sercey, G., Heikal, M.R., and Gold, M., *12th Triennial International Conference on Liquid Atomization and Spray Systems*, Heidelberg, Germany, September 2012.
22. Engine Combustion Network website. http://www.sandia.gov/ecn/index.php.
23. Otsu, N., *IEEE Transactions on Systems, Man, and Cybernetics* 9:62-66 (1979).
24. Naber, J., and Siebers, D., SAE Technical Paper 960034 (1996).
25. Reitz, R.D., and Bracco, F.V., *Physics of Fluids* 25:1730-1742 (1982).
26. Siebers, D.L., SAE Technical Paper 1999-01-0528 (1999).